PCCP

PAPER

View Article Online
View Journal | View Issue

Check for updates

Cite this: *Phys. Chem. Chem. Phys.*, 2026, **28**, 4314

Direct *in situ* detection of grain boundary reduction in nanocrystalline ceria

Claire M. Donahue, [a] Qing Ma [b] and Sossina M. Haile *[a]

Received 26th September 2025,
Accepted 25th January 2026

DOI: 10.1039/d5cp03733f

rsc.li/pccp

Enrichment of the reduced Ce^{3+} species near grain boundaries in ceria is a widely established phenomenon which has previously been observed in *ex situ* experiments. Here, *in situ* X-ray absorption near-edge spectroscopy (XANES) is employed to detect and quantify grain boundary reduction under device-relevant conditions. Single-crystal and dense nanocrystalline films of undoped ceria were characterized by Ce L_3 XANES at high temperatures (615–845 °C) in humidified hydrogen. Nanocrystalline ceria (30–40 nm mean grain sizes) exhibited large enhancements in Ce^{3+} concentration, from 2.0× to 11× relative to bulk ceria. Implications for grain boundary reduction thermodynamics and anticipated conductivity enhancements are discussed.

Open Access Article. Published on 26 January 2026. Downloaded on 5/10/2026 7:56:44 AM.
This article is licensed under a Creative Commons Attribution-NonCommercial 3.0 Unported Licence.

Introduction

Ceria (CeO_2 and doped derivatives) plays a crucial role in existing and emerging technologies in the areas of heterogeneous catalysis and energy storage and conversion. A key feature of the physical chemistry of ceria is the highly accessible and reversible Ce^{4+}/Ce^{3+} redox couple, described according to the following reaction:

$$2Ce_{Ce}^{\times} + O_O^{\times} \rightleftarrows 2Ce'_{Ce} + V_O^{\bullet\bullet} + \frac{1}{2}O_2(g)$$

where $Ce_{Ce}^{\times}$ is the effectively neutral Ce^{4+} species and Ce'_{Ce} is the Ce^{3+} species with effective negative charge.[1] Significantly, the extent of reduction of ceria is known to be higher at interfaces than within the bulk of the material. This includes gas-solid interfaces (surfaces),[2–10] interfaces with metals[11] or other oxides[12] (heterointerfaces), and internal interfaces (grain boundaries).[13–15] Interfacial reduction has important implications for the functional properties of ceria. When acceptor-doped ceria is employed as an electrolyte for its high ionic $(V_O^{\bullet\bullet})$ conductivity, enhanced Ce^{3+} at the grain boundaries is undesirable due to its association with space charge effects that deplete oxygen vacancies in the vicinity of the boundary.[16–18] In undoped nanocrystalline ceria, grain boundary reduction results in enhanced electronic (Ce'_{Ce}) conductivity relative to bulk behavior.[19–22] When employed as a catalyst or catalyst support, surface vacancies are desirable catalytic sites[8,23] and thus surface reduction, where Ce^{3+} is presumed to be compensated by oxygen vacancies, is favorable. The detailed relationships between these various properties and defect chemistry remain murky because defect concentrations at interfaces, particularly under application-relevant conditions, are difficult to quantify. Moreover, at the very small length scales that define interface behavior, electroneutrality may be violated, and thus Ce'_{Ce} and $V_O^{\bullet\bullet}$ need not be present in direct proportion within the region of interest.

Enhanced reduction of ceria interfaces has been evidenced by several direct experimental studies. Both grain boundaries and surfaces in ceria have been characterized extensively by scanning transmission electron microscopy (STEM) methods, primarily by detection of Ce^{3+} *via* electron energy loss spectroscopy (EELS).[4–6,13–15] Surface reduction has furthermore been established by X-ray photoelectron spectroscopy (XPS).[6] Both STEM and XPS are traditionally limited to high vacuum and ambient or low temperatures, but advances in differential pumping have enabled these methods to be utilized at conditions approaching those employed in operational devices. In particular, near-ambient XPS (NAXPS) has been exploited to quantify Ce^{3+} concentrations at surfaces.[7–9] More recently, we have utilized grazing-incidence X-ray absorption near-edge spectroscopy (XANES)[2,3] to gain access to the cerium oxidation state at surfaces under truly device-relevant conditions. Because XANES is entirely an X-ray method, differential pumping is not required, and the experimental configuration is readily integrated with environmental chambers for temperature and gas control, enabling true *in situ* studies. Moreover, by using thin-film samples and controlling the X-ray incidence angle α, one can achieve both full-film sensitivity and surface sensitivity (top 2–3 nm).

The present work is focused on *in situ* detection of Ce^{3+} at the grain boundaries of undoped ceria. Dense nanocrystalline ceria (grain size 25–45 nm) (Fig. 1 and Fig. S1, S2) is characterized using Ce L_3 edge XANES, providing an aggregate measurement

[a] *Department of Materials Science and Engineering, Northwestern University, Evanston, IL, 60208, USA. E-mail: sossina.haile@northwestern.edu*
[b] *Dow-Northwestern-Dupont Collaborative Access Team, Synchrotron Research Center, Argonne, USA*

 This journal is © the Owner Societies 2026

Open Access Article. Published on 26 January 2026. Downloaded on 5/10/2026 7:56:44 AM.
This article is licensed under a Creative Commons Attribution-NonCommercial 3.0 Unported Licence.

of grain boundary chemistry. The measurements are carried out at high temperatures and low oxygen partial pressures (pO_2), conditions similar to those at which enhanced electronic conductivities have been reported.[20,21] The behavior of the dense nanocrystalline CeO_2 film is compared to that of a single-crystal CeO_2(100) film. We observe significant excess reduction in the nanocrystalline film, the first direct *in situ* evidence of grain boundary reduction under device relevant conditions, and quantify the level of Ce^{3+} enrichment on a per-boundary-area basis.

Results and analysis

Three conditions were selected for XANES measurements: (1) T = 615 °C and $pO_2 = 1.0 \times 10^{-24}$ atm, (2) T = 845 °C and $pO_2 = 9.9 \times 10^{-19}$ atm, and (3) T = 845 °C and $pO_2 = 1.2 \times 10^{-19}$ atm, where the low oxygen partial pressure is achieved through H_2/H_2O mixtures. At these conditions, moderate Ce reduction is expected in the bulk (from 0.2 to 7%), and thus the relative impact of grain boundary reduction can be expected to be sufficiently large for detection. Full-film-sensitive spectra were collected at an incidence angle of $\alpha = 9.5^\circ$ for the nanocrystalline CeO_2 film (Fig. 2a–c). The single-crystal CeO_2 film was measured under condition #2 in both the full-film geometry and in a grazing-incidence geometry at $\alpha = 0.23^\circ$, below the critical angle of $\sim 0.45^\circ$ (Fig. 2d and e). The latter was used to establish the extent of surface reduction. All spectra were analyzed using linear combination (LC) fitting against Ce^{4+} and Ce^{3+} reference spectra collected as part of this work. The fitting procedure extends beyond conventional LC fitting by including a treatment of self-absorption effects, as detailed in the supplemental information.

Full-film XANES spectra at a temperature of 845 °C and an oxygen partial pressure of 9.9×10^{-19} atm (condition #2) directly reveal a higher concentration of Ce^{3+} in the nanocrystalline CeO_2 than in the single-crystal CeO_2 (Fig. 3). The enhanced reduction in the nanocrystalline film is evident in the shift in edge position towards lower energy. The spectra indicate that the presence of grain boundaries results in a two-fold enhancement of cerium reduction, with Ce^{3+} concentrations of 9.7% and 4.7%, respectively, in the nanocrystalline and single-crystal films.

Because the full-film measurements ($\alpha = 9.5^\circ$) are sensitive to surface reduction,[2,3] in addition to reduction in the interior of the film, they cannot be directly used to quantify grain boundary reduction. To convert the $c_{\text{film effective}}$ values obtained by LC fitting to the Ce^{3+} concentration in the bulk of the film, $c_{\text{film bulk}}$, we make use of the surface measurement of the single-crystal film. Although the nanocrystalline film includes a variety of terminations, our prior work has established that, under an environment similar to those employed here, the {100}, {110}, and {111} terminations exhibit similar extents of surface reduction.[3] Thus, the surface reduction of the (100)-terminated single-crystal film, which was sufficiently smooth to enable surface sensitivity in the grazing incidence geometry, is a suitable proxy for surface reduction in the nanocrystalline film. The nanocrystalline film surface was too rough for direct characterization.

The conversion of $c_{\text{film effective}}$ to $c_{\text{film bulk}}$ is achieved by approximating the Ce^{3+} concentration profile of the single-crystal film as a step function (roughly similar to observed surface reduction profiles, such as that of Turner *et al.*[4]) in which the surface is fully reduced (100% Ce^{3+}) to a depth of ℓ_{surf}, while the Ce^{3+} level in the remainder of the film is $c_{\text{film bulk}}$. Our analysis (as detailed in the supplemental information) yields $\ell_{\text{surf}}^{\text{single}X} = 2.0\,\text{nm}$ and $c_{\text{film bulk}}^{\text{single}X}$ = 3.6% in condition #2.

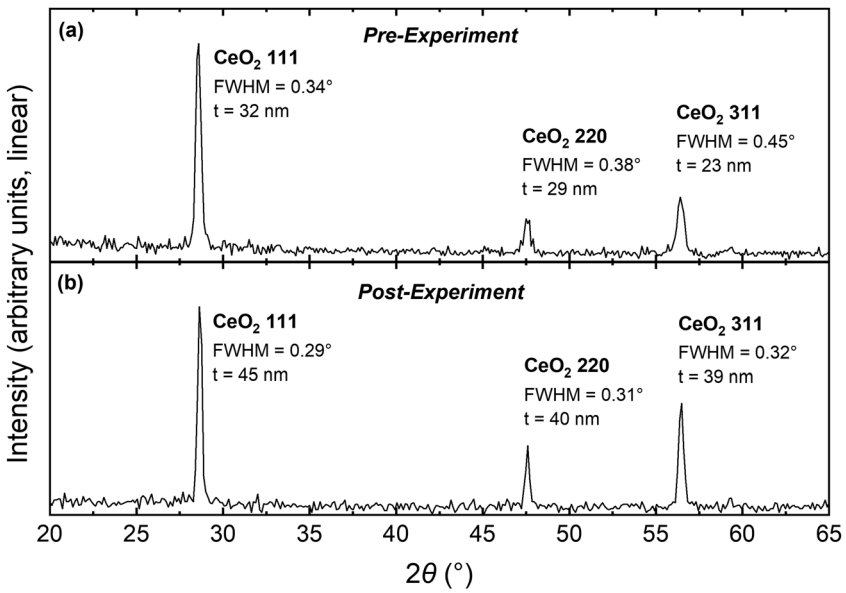

Fig. 1 Specular X-ray diffractometry (Cu K_α source, λ = 1.541 Å) of the nanocrystalline CeO_2 film (a) prior to XANES experiment, following deposition and annealing at 625 °C, and (b) after XANES experiment with a maximum temperature of 845 °C. The full-width-half-maximum (FWHM) in 2θ is indicated for each Bragg reflection, and out-of-plane crystallite sizes (t) were calculated using the Scherrer equation.

Open Access Article. Published on 26 January 2026. Downloaded on 5/10/2026 7:56:44 AM.
This article is licensed under a Creative Commons Attribution-NonCommercial 3.0 Unported Licence.

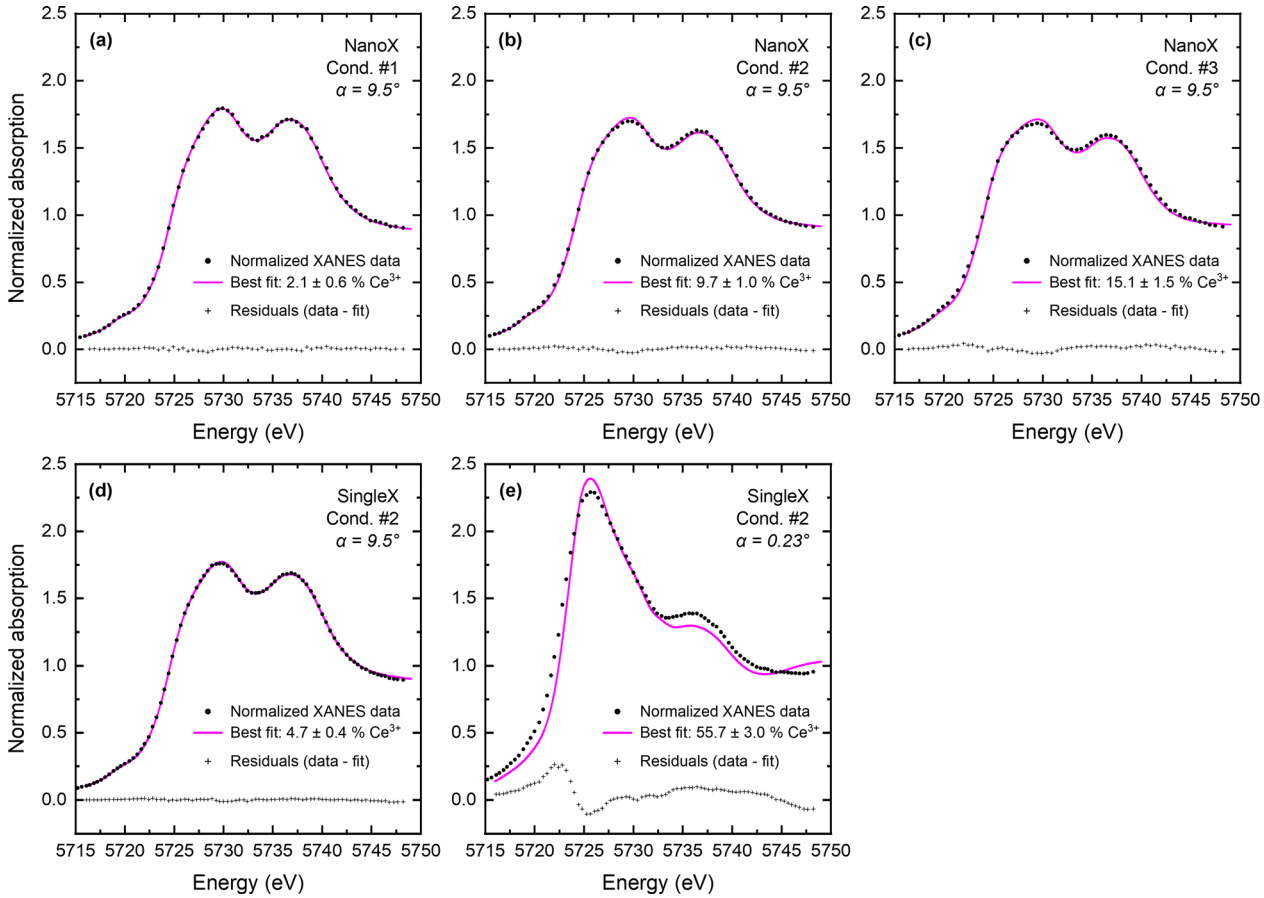

Fig. 2 Data, fitted curves, and residuals for all experimental normalized XANES spectra. (a)–(c) nanocrystalline CeO_2 measured in full-film geometry ($\alpha = 9.5^\circ$) in three conditions. (d) and (e) single-crystal CeO_2 under condition #2 measured in full-film ($\alpha = 9.5^\circ$) (d) and surface ($\alpha = 0.23^\circ$) (e) geometry. Ce^{3+} content (c', where $c' = c_{\text{film effective}}$ in full-film cases) was characterized by linear combination fitting to the Ce^{3+} and Ce^{4+} reference spectra; see text for a complete description of data analysis procedures. Condition #1: T = 615 °C, $pO_2 = 1.0 \times 10^{-19}$ atm. Condition #2: T = 845 °C, $pO_2 = 9.9 \times 10^{-19}$ atm. Condition #3: T = 845 °C, $pO_2 = 1.2 \times 10^{-19}$ atm.

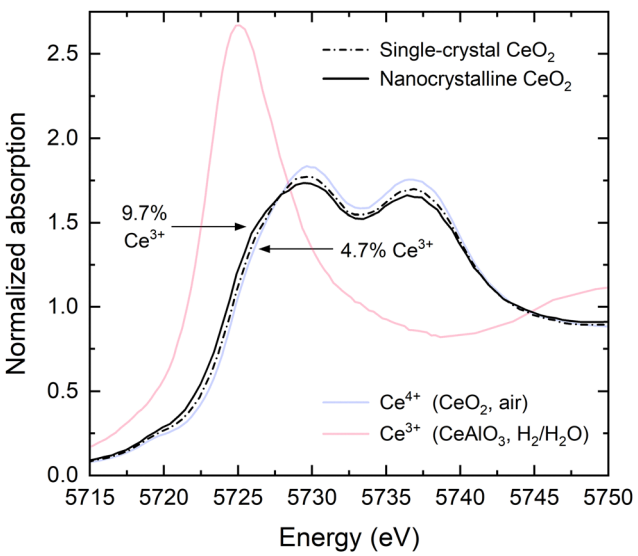

Fig. 3 Direct comparison of the normalized XANES spectra for single-crystal ($c_{\text{film effective}}$ = 4.7% Ce^{3+}) and nanocrystalline CeO_2 ($c_{\text{film effective}}$ = 9.7% Ce^{3+}) films at 845 °C and $pO_2 = 9.9 \times 10^{-19}$ atm (condition #2), measured at an incidence angle of 9.5° for full-film sensitivity. The nanocrystalline film displays substantially enhanced reduction relative to the single-crystal film.

While the true Ce^{3+} profile may differ from the step-function approximation, determination of $c_{\text{film bulk}}$ was found to be relatively insensitive to the functional form of the profile. The derived $c_{\text{film bulk}}^{\text{single}X}$ value is in reasonable agreement with the expected Ce^{3+} concentration for bulk ceria at T = 845 °C and $pO_2 = 9.9 \times 10^{-19}$ atm, 3.2%.[24] Surface reduction in this 220 nm thick single-crystal film therefore accounts for a minor, but significant, portion of the full-film concentration, with a 23% difference between $c_{\text{film effective}}$ and $c_{\text{film bulk}}$. Assuming a reduced surface layer of the same thickness in the nanocrystalline CeO_2 film (with a total thickness of 315 nm) under the same condition, we calculate the extent of reduction in the bulk of the film, $c_{\text{film bulk}}^{\text{nano}X}$, to be 9.0%, as compared to $c_{\text{film effective}}^{\text{nano}X}$ = 9.7%. In this case, surface reduction contributes less than 10% of the Ce^{3+} species in the entire film.

For treatment of the nanocrystalline film in the other two conditions, we make the plausible assumption that the fraction of the total Ce^{3+} concentration due to surface reduction is fixed. Because the correction to $c_{\text{film effective}}^{\text{nano}X}$ to obtain $c_{\text{film bulk}}^{\text{nano}X}$ was found to be relatively small in condition #2, even moderate variations in the ratio of $c_{\text{film effective}}$ to $c_{\text{film bulk}}$ have only a small

 This journal is © the Owner Societies 2026

Open Access Article. Published on 26 January 2026. Downloaded on 5/10/2026 7:56:44 AM.
This article is licensed under a Creative Commons Attribution-NonCommercial 3.0 Unported Licence.

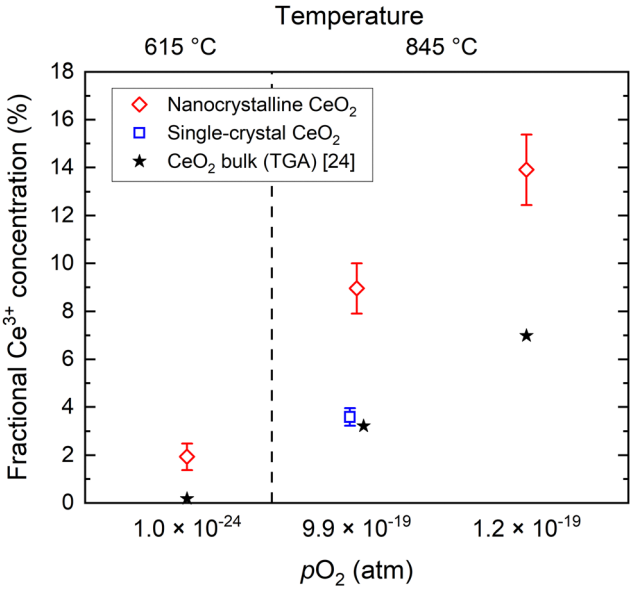

Fig. 4 Fractional Ce^{3+} concentrations ($c_{\text{film bulk}}$) determined by XANES in nanocrystalline and single-crystal CeO_2 films under high-temperature reducing conditions. The expected equilibrium Ce^{3+} concentration for bulk CeO_2 is calculated from (T, pO_2) for each condition according to published TGA data.[24]

impact on the value of $c_{\text{film bulk}}$, introducing errors that lie within the overall uncertainty of the measurement.

The residuals from LC fitting to the XANES spectra, included in Fig. 2, are relatively small for the full-film measurements but notably large for the surface measurement (Fig. 2e) in which the Ce^{3+} concentration is large. The origin of this discrepancy is readily attributed to the difference between the coordination environment of Ce^{3+} within the fluorite crystal structure of ceria (coordination number 8) and that within the $CeAlO_3$ reference (coordination number 12).[26] This attribution is corroborated by the fact that the residuals across all five XANES spectra scale linearly with the fitted Ce^{3+} concentration (Fig. S6). The reported uncertainties in Ce^{3+} concentration account for this limitation of the LC fitting. We emphasize that the residuals (and hence uncertainties) are small for all nanocrystalline ceria measurements and note that the conversion of $c^{\text{nano}X}_{\text{film effective}}$ to $c^{\text{nano}X}_{\text{film bulk}}$ is largely insensitive to the precise value of the surface reduction within the uncertainty range obtained for this quantity.

The Ce^{3+} content in nanocrystalline ceria ($c^{\text{nano}X}_{\text{film bulk}}$), as compared to single-crystal or bulk ceria, is shown in Fig. 4 and Table 1 for all three conditions. In the conditions where no single-crystal measurement was performed, the expected bulk Ce^{3+} concentration for undoped ceria is taken from thermogravimetric analysis (TGA) data[24] for the given T and pO_2. In all three conditions, the results demonstrate a substantial enhancement of Ce^{3+} content in nanocrystalline ceria as compared to bulk ceria. Notably, the enhancement effect is not uniform for the three conditions. At 845 °C, grain boundary reduction increases roughly in proportion to bulk reduction by a factor between 2 and 2.5 in conditions #2–3, whereas at 615 °C (condition #1), at which little bulk reduction occurs (0.2% Ce^{3+}), the enhancement factor is 11.

To interpret grain boundary reduction in the nanocrystalline CeO_2 film, we apply a form of the brick-layer model with fully reduced grain boundary regions, analogous to the treatment of surface reduction. The sample is represented by cubic grain interiors (side length $t_{\text{grain}} - \ell_{\text{GB}}$), having the equilibrium bulk Ce^{3+} concentration ($c_{\text{CeO}_2\text{ bulk}}$), that are separated by grain boundaries of width ℓ_{GB}, with a Ce^{3+} concentration of 100%. The average crystallite size, t_{grain}, is obtained from XRD (Fig. 1). For condition #1 at 615 °C, where no grain growth is expected, we use the pre-experiment value, and for conditions #2 and #3 at 845 °C, where grain growth is assumed to be complete prior to the measurement, we use the post-experiment value. Based on the volume fraction of fully-reduced and bulk-like regions, we compute ℓ_{GB} according to:

$$\ell_{\text{GB}} = t_{\text{grain}}\left(1 - \sqrt[3]{\frac{1 - c^{\text{nano}X}_{\text{film bulk}}}{1 - c_{\text{CeO}_2\text{ bulk}}}}\right) \quad (1)$$

The value of $c_{\text{CeO}_2\text{ bulk}}$ is taken from published thermogravimetric analysis (TGA) data[24] for the given T and pO_2, except in the case of condition #2, for which our measured $c^{\text{single}X}_{\text{film bulk}}$ value is used. While the grain boundary reduction profile, as with the surface reduction profile, is unlikely to be a precise step function between partially and fully reduced ceria, ℓ_{GB} (and, analogously, ℓ_{surf} for surface reduction) serves to quantify area-normalized interfacial reduction regardless of the exact profile.

As summarized in Table 1, we find the width of grain boundary reduction (ℓ_{GB}) in nanocrystalline CeO_2 to be 0.17 nm in condition #1, at which bulk reduction is lowest, 0.78 nm in condition #2, and 1.1 nm in condition #3, at which bulk reduction is greatest. Thus, while there are differences in grain size and hence grain boundary density, the grain boundary reduction trend follows the bulk reduction trend, though not with a uniform scaling factor. Furthermore, the results in condition #2 (845 °C, $pO_2 = 9.9 \times 10^{-19}$ atm, $c_{\text{CeO}_2\text{ bulk}} = 3.6\%$) allow for direct comparison of grain boundary reduction to surface reduction. Ce^{3+} enrichment is observed at both types of interface, with the effect being approximately 2.5× as extensive

Table 1 Experimental results and derived quantities, defined in text, for nanocrystalline CeO_2 under three reducing conditions

Condition	T, °C	pO_2, atm	t_{grain}, nm	$c_{\text{film bulk}}$	$c_{\text{CeO}_2\text{ bulk}}$	ℓ_{GB}, nm	ℓ_{surf}, nm
#1	615	1.0×10^{-24}	29	1.9 ± 0.6%	0.2%[a]	0.17	—
#2	845	9.9×10^{-19}	41	9.0 ± 1.0%	3.6%[b]	0.78	2.0
#3	845	1.2×10^{-19}	41	13.9 ± 1.5%	7.0%[a]	1.1	—

[a] Calculated by TGA data[24] from T and pO_2. [b] Determined experimentally, equal to $c^{\text{single}X}_{\text{film bulk}}$.

Open Access Article. Published on 26 January 2026. Downloaded on 5/10/2026 7:56:44 AM. This article is licensed under a Creative Commons Attribution-NonCommercial 3.0 Unported Licence.

at the (100) surface compared to the grain boundaries ($\ell_{surf} = 2.0$ nm, $\ell_{GB} = 0.78$ nm).

Discussion

The magnitude of grain boundary reduction in condition #1, while significantly lower than the values observed in conditions #2 and #3, is comparable to that reported under high vacuum at room temperature.[13,14] EELS studies by Feng and Hojo *et al.* find that Ce^{3+} levels vary between grain boundary orientations, with some exhibiting zero reduction and others exhibiting roughly 10 to 40% Ce^{3+}.[13,14,25] Analysis of the three grain boundaries ℓ_{GB} with nonzero Ce^{3+} content in ref. 13 indicates the spatial extent of Ce^{3+} reduction of these boundaries to be between approximately 0.1 and 0.3 nm.

The fact that grain boundary reduction in condition #1 is not significantly higher than *ex situ* results, despite the much more strongly reducing environment in our measurement, is somewhat surprising. We speculate that Ce^{3+} enhancement at grain boundaries occurs at an approximately fixed baseline level over a wide range of conditions and becomes more extensive in conditions producing measurable bulk reduction, with an onset point spanned by the conditions of this study. In such a scenario, condition #1 produces only the baseline reduction. Analogous behavior appears to describe surface reduction in ceria, which occurs to an approximately fixed extent under a range of conditions—vacuum at room temperature,[4–6] air at room temperature,[2,3,6] and air at high temperature[2]—before increasing to a larger value at high temperature and low oxygen partial pressure.[2,3] Under *ex situ* STEM conditions, Ce^{3+} enrichment near grain boundaries has been observed in conjunction with oxygen vacancies at low-coordination sites that are structurally necessary for certain grain boundary orientations.[13] This behavior could account for the baseline level of grain boundary reduction. Generation of additional vacancies in the grain boundary region presumably requires removal of more stable oxygen species and thus corresponds to conditions which also drive measurable reduction in the bulk.

The results obtained here can also be considered in the context of the widely accepted space-charge model of ceria grain boundary behavior, in which a positively charged grain boundary core is balanced by a neighboring space charge region where oxygen vacancies are depleted and the Ce^{3+} concentration is enhanced. If a space charge model is applied to the present results, observation of such a large decrease in relative-to-bulk grain boundary reduction, despite the increase on an absolute basis, from condition #1 (615 °C) to conditions #2–3 (845 °C) would likely require a decrease in the space charge potential.

The community interest in ceria grain boundary reduction is largely driven by observations of high electronic conductivity in nanocrystalline ceria. In the absence of detailed knowledge of the Ce^{3+} concentration profile and the effective electronic mobility in the grain boundary region, it is impossible to predict with high confidence the conductivity expected for the nanoceria film studied here. Nevertheless, reasonable estimates of the conductivity enhancements in the three conditions can be made by the following approach. We first consider the measured Ce^{3+} concentration ($c_{film\,bulk}$) as if it is spatially uniform throughout the nanocrystalline film rather than concentrated near grain boundaries. From the measured $c_{film\,bulk}$ values (Table 1) and the reported thermodynamic properties of ceria,[24] we obtain equivalent oxygen partial pressures at which these $c_{film\,bulk}$ values would be obtained: 2.9×10^{-29}, 7.0×10^{-20}, and 2.7×10^{-20} atm for conditions #1–3, respectively. We then estimate the conductivities at these implied conditions. The conductivity of undoped ceria in high-temperature reducing conditions follows a $pO_2^{-1/n}$ power law behavior, where the value of n falls between 4 and 6 as explained by the defect chemistry.[27] Taking n = 6, the experimentally observed value at the equivalent pO_2 values, the increase in conductivity due to a decrease in oxygen partial pressure from the actual to equivalent values approaches 500% for condition #1. For conditions #2 and #3, however, it is much lower, approximately 50% and 25%, respectively. Thus, the greater differential between bulk and grain boundary reduction observed in condition #1 corresponds to a greater differential in conductivity as compared to the other two conditions. A more realistic spatial distribution of Ce^{3+}, in which the Ce^{3+} concentration is enhanced only in the vicinity of grain boundaries, is treated in the SI and reveals that conductivity enhancement is expected to be even lower in such cases. This is due to the dependence of the electronic conductivity in ceria on Ce^{3+} concentration, which rises steeply at low Ce^{3+} concentrations before leveling out near the spatially-averaged concentrations in the film ($c_{film\,bulk}$) and ultimately decreasing with concentration above ~25% Ce^{3+}.[28] Therefore, the enhancement factors reported above are taken as upper-bound estimates.

Comparison of these predictions to experimental studies of conductivity in nanocrystalline ceria are challenging due to differences in grain sizes, unknown impurity levels, and unknown substrate-film interfacial effects, which have led to a wide variation in the reported enhancement factors. Nevertheless, we note that Kosacki *et al.*[20] report a 10× enhancement in thin films (several 100 nm in thickness, 30 nm grain size) at 600 °C and 10^{-24} atm pO_2, whereas Göbel *et al.*[22] report a ~2× enhancement at 700 °C and 1 atm pO_2 (films 50 to 200 nm in thickness, with mean grain sizes from 16 to 38 nm). These conductivities, with a very large enhancement under reducing conditions and a minimal enhancement under mild conditions, appear counter to the present analysis. On the other hand, Kogut *et al.*[21] report a large enhancement (as measured from ~2 μm thick films with mean grain size of 54 nm) under mild conditions, about a factor of 15 under air, which falls to effectively no enhancement at low pO_2 for temperatures from 600 to 900 °C, a result that agrees with our predictions. While lateral conductivity measurements were precluded in our work due to the non-negligible conductivity of the Si substrate, the methodology developed here is well-suited for combined evaluation of Ce^{3+} concentration and conductivity using suitably insulating substrates.

Conclusions

By *in situ* XANES characterization of the cerium oxidation state, we report direct quantitative evidence of grain boundary

 This journal is © the Owner Societies 2026

Open Access Article. Published on 26 January 2026. Downloaded on 5/10/2026 7:56:44 AM.
This article is licensed under a Creative Commons Attribution-NonCommercial 3.0 Unported Licence.

reduction in ceria under high-temperature reducing conditions. Dense nanocrystalline CeO_2 (with mean grain sizes in the 30 to 40 nm range) exhibits substantial enhancement in total concentration of the reduced Ce^{3+} species over that in single-crystal CeO_2, where the enhancement factor, ranging from 2.0 to 11, decreases with increasing Ce^{3+} concentration in the bulk. The width of the reduced grain boundary region, using a simplified brick-layer model in which Ce near the boundary is entirely in the 3+ oxidation state, is calculated to be 0.17 nm, 0.78 nm, and 1.1 nm in each of the three conditions studied, from least to most bulk-reducing. Under the central condition, we also characterized the related phenomenon of surface reduction in single-crystal CeO_2(100) and found it to be roughly 2.5× as extensive as grain boundary reduction. The diminishing enhancement factor for grain boundary reduction as bulk reduction increases is tentatively explained by the presence of a baseline concentration of structurally necessary oxygen vacancies at grain boundaries. Beyond this, additional vacancies in the grain boundary region are generated under redox conditions which also drive substantial bulk reduction. While electronic conductivity, generally observed to be enhanced by Ce^{3+} enrichment at grain boundaries, was not measured in this study, we predict that the conductivity enhancement factor decreases with increasing bulk reduction, in line with the factor of Ce^{3+} enhancement.

Methods

The dense nanocrystalline CeO_2 film, 315 nm in thickness as measured by ellipsometry, was grown on an Si(100) substrate by pulsed laser deposition (PLD) (KrF 248 nm excimer laser, 1.4 J cm^{-2} laser energy, 10 Hz repetition rate, room temperature, base pressure) and then annealed at 625 °C in air for 14 hours. The film is polycrystalline with a slight preferential orientation along (111) and an absence of (100)-oriented grains, as evidenced by specular X-ray diffraction (XRD) both before and after the XANES experiments (Fig. 1). Crystallite sizes, t, were determined from the full-width-half-maximum (FWHM) for each of the three observed XRD peaks, after subtracting instrumental broadening ($FWHM_{instrument}$ = 0.22°, determined by XRD of 5 μm-sized CeO_2 powder), by the Scherrer equation (K = 0.9).[29] The effective grain size, t_{grain}, is calculated as the weighted average of the three t values, where the weights are determined by comparison of peak intensities to randomly-oriented CeO_2. The analysis yields t_{grain} = 28.5 nm pre-experiment and t_{grain} = 41.4 nm post-experiment (grain growth due to elevated temperature in experiment). Following the XANES experiment, surface morphology was characterized by atomic force microscopy (AFM) (Fig. S1) and film density was assessed by X-ray reflectivity (XRR) (Fig. S2). The AFM root-mean-square roughness (1.6 nm) and the XRR density (99 ± 5% of theoretical) indicate that the CeO_2 film is dense and non-porous, such that internal surfaces are not present in any consequential amount.

The oriented single-crystal CeO_2(100) film, 220 nm in thickness, was grown on a $Y_{0.16}Zr_{0.84}O_{1.92}$ (yttria-stabilized zirconia, YSZ) (100) substrate by PLD (KrF 248 nm excimer laser, 1.7 J cm^{-2} laser energy, 10 Hz repetition rate, 625 °C, 15 mTorr O_2) and then annealed at 950 °C in flowing oxygen for 2.5 hours. XRD shows the film to be fully (100)-oriented with high crystallinity (Fig. S3), and AFM shows the film surface to be sufficiently smooth (0.57 nm root-mean-square roughness) for the surface-sensitive XANES technique (Fig. S4).

XANES experiments were conducted at the DND-CAT 5-BM-D station at the Advanced Photon Source of Argonne National Laboratory. The incident X-ray beam energy was controlled by an Si(111) double-crystal monochromator with an energy resolution of $\Delta E/E = 1.4 \times 10^{-4}$. Two Hitachi Vortex-ME4 silicon drift detectors, set at 90° relative to the beam path, were used to collect the Ce fluorescence signal which was divided by the incident beam intensity to yield the raw absorption data. Each Ce L_3 XANES spectrum was normalized, by linear fitting to pre- and post-edge regions, to set the absorption edge height to unity. Gas and temperature conditions were controlled using an Anton Paar domed hot stage (DHS1100). Gas composition was 3.5% H_2 (condition #1–2) or 10% H_2 (condition #3), balance He, passed through liquid water held at 15 °C to establish light humidity (pH_2O = 0.017). pO_2 is determined by pH_2O, pH_2, and T according to the equilibrium of the water dissociation reaction at the sample surface.[30]

There is some subtlety in extracting Ce^{3+} concentrations from the XANES measurements. The fractional Ce^{3+} character of a given XANES spectrum, c', is an average across all Ce absorption events in the sample and is inherently weighted toward low depths due to X-ray attenuation. In full-film XANES, at a relatively high incidence angle, the attenuation with depth is minimal compared to film thickness, and c' is taken to equal the Ce^{3+} concentration across the entirety of the film, $c_{film\ effective}$. In surface XANES, the c' value heavily reflects near-surface behavior and is interpreted using a more rigorous analysis to determine $c_{film\ bulk}$ and ℓ_{GB} (see SI). In either case, c' values are determined by fitting experimental XANES data to a linear combination (LC) of reference spectra for Ce^{3+} ($\mu_{Ce^{3+}}(E)$) and Ce^{4+} ($\mu_{Ce^{4+}}(E)$):

$$\mu_{LC}(E) = (c')\mu_{Ce^{3+}}(E) + (1 - c')\mu_{Ce^{4+}}(E) \quad (2)$$

To account for minor self-absorption effects, two additional fit parameters are included in the LC fitting (see SI). The complete expression (eqn (S4)) is fitted to the experimental XANES data in the energy range 5715 to 5750 eV by nonlinear least-squares regression. The resulting c' values are obtained with uncertainty defined by their 95% confidence intervals. The reference spectra were collected at 800 °C using CeO_2 in air (Ce^{4+} reference) and $CeAlO_3$ in humidified hydrogen (Ce^{3+} reference).[31–33]

Conflicts of interest

There are no conflicts to declare.

Data availability

The data supporting this article have been included as part of the supplementary information (SI). Supplementary information is

Open Access Article. Published on 26 January 2026. Downloaded on 5/10/2026 7:56:44 AM. This article is licensed under a Creative Commons Attribution-NonCommercial 3.0 Unported Licence.

available. See DOI: https://doi.org/10.1039/d5cp03733f. These data are also available at https://doi.org/10.17605/OSF.IO/JNKC3.

Acknowledgements

This work was supported by the U.S. National Science Foundation (NSF) under award DMR-2130831. The XANES experiments were performed at the DuPont-Northwestern-Dow Collaborative Access Team (DND-CAT) located at Sector 5 of the Advanced Photon Source (APS). DND-CAT is supported by Northwestern University, The Dow Chemical Company, and DuPont de Nemours, Inc. This research used resources of the Advanced Photon Source, a U.S. Department of Energy (DOE) Office of Science User Facility operated for the DOE Office of Science by Argonne National Laboratory under Contract No. DE-AC02-06CH11357. This work made use of the Jerome B. Cohen X-ray Diffraction Core Facility (RRID:SCR_017866) and the Pulsed Laser Deposition Shared Facility (RRID:SCR_017889) at the Materials Research Center at Northwestern University, supported by the MRSEC program (NSF DMR-2308691) and the Soft and Hybrid Nanotechnology Experimental (SHyNE) Resource (NSF ECCS-2025633). This work made use of the SPID facility of Northwestern University's NUANCE Center, which has received support from the SHyNE Resource (NSF ECCS-2025633), the IIN, and Northwestern's MRSEC program (NSF DMR-2308691).

References

1 R. Schmitt, A. Nenning, O. Kraynis, R. Korobko, A. I. Frenkel, I. Lubomirsky, S. M. Haile and J. L. M. Rupp, *Chem. Soc. Rev.*, 2019, **49**, 554.
2 W. Yuan, Q. Ma, Y. Liang, C. Sun, K. V. L. V. Narayanachari, M. J. Bedzyk, I. Takeuchi and S. M. Haile, *J. Mater. Chem. A*, 2020, **8**, 9850.
3 W. Yuan and S. M. Haile, *MRS Commun.*, 2020, 1.
4 S. Turner, S. Lazar, B. Freitag, R. Egoavil, J. Verbeeck, S. Put, Y. Strauven and G. V. Tendeloo, *Nanoscale*, 2011, **3**, 3385.
5 X. Hao, A. Yoko, C. Chen, K. Inoue, M. Saito, G. Seong, S. Takami, T. Adschiri and Y. Ikuhara, *Small*, 2018, **14**, 1802915.
6 F. Zhang, P. Wang, J. Koberstein, S. Khalid and S.-W. Chan, *Surf. Sci.*, 2004, **563**, 74.
7 W. C. Chueh, A. H. McDaniel, M. E. Grass, Y. Hao, N. Jabeen, Z. Liu, S. M. Haile, K. F. McCarty, H. Bluhm and F. E. Gabaly, *Chem. Mater.*, 2012, **24**, 1876.
8 Z. A. Feng, F. E. Gabaly, X. Ye, Z.-X. Shen and W. C. Chueh, *Nat. Commun.*, 2014, **5**, 4374.
9 C. B. Gopal, F. E. Gabaly, A. H. McDaniel and W. C. Chueh, *Adv. Mater.*, 2016, **28**, 4692.
10 A. F. Zurhelle, X. Tong, A. Klein, D. S. Mebane and R. A. D. Souza, *Angew. Chem., Int. Ed.*, 2017, **56**, 14516.
11 P. Luches, L. Giordano, V. Grillo, G. C. Gazzadi, S. Prada, M. Campanini, G. Bertoni, C. Magen, F. Pagliuca, G. Pacchioni and S. Valeri, *Adv. Mater. Interfaces*, 2015, **2**, 1500375.
12 K. Song, H. Schmid, V. Srot, E. Gilardi, G. Gregori, K. Du, J. Maier and P. A. van Aken, *APL Mater.*, 2014, **2**, 032104.
13 B. Feng, I. Sugiyama, H. Hojo, H. Ohta, N. Shibata and Y. Ikuhara, *Sci. Rep.*, 2016, **6**, 20288.
14 H. Hojo, T. Mizoguchi, H. Ohta, S. D. Findlay, N. Shibata, T. Yamamoto and Y. Ikuhara, *Nano Lett.*, 2010, **10**, 4668.
15 Y. Lei, Y. Ito, N. D. Browning and T. J. Mazanec, *J. Am. Ceram. Soc.*, 2002, **85**, 2359.
16 S. Kim, J. Fleig and J. Maier, *Phys. Chem. Chem. Phys.*, 2003, **5**, 2268.
17 H. J. Avila-Paredes, K. Choi, C.-T. Chen and S. Kim, *J. Mater. Chem.*, 2009, **19**, 4837.
18 E. C. C. Souza, W. C. Chueh, W. Jung, E. N. S. Muccillo and S. M. Haile, *J. Electrochem. Soc.*, 2012, **159**, K127.
19 M. Chiang, E. B. Lavik, I. Kosacki, H. L. Tuller and J. Y. Ying, *Appl. Phys. Lett.*, 1996, **69**, 185.
20 I. Kosacki, T. Suzuki, V. Petrovsky and H. U. Anderson, *Solid State Ionics*, 2000, **136**, 1225.
21 I. Kogut, C. Steiner, H. Wulfmeier, A. Wollbrink, G. Hagen, R. Moos and H. Fritze, *J. Mater. Sci.*, 2021, **56**, 17191.
22 M. C. Göbel, G. Gregori, X. Guo and J. Maier, *Phys. Chem. Chem. Phys.*, 2010, **12**, 14351.
23 T. Montini, M. Melchionna, M. Monai and P. Fornasiero, *Chem. Rev.*, 2016, **116**, 5987.
24 R. J. Panlener, R. N. Blumenthal and J. E. Garnier, *J. Phys. Chem. Solids*, 1975, **36**, 1213.
25 B. Feng, H. Hojo, T. Mizoguchi, H. Ohta, S. D. Findlay, Y. Sato, N. Shibata, T. Yamamoto and Y. Ikuhara, *Appl. Phys. Lett.*, 2012, **100**, 073109.
26 Y. Takahashi, H. Sakami and M. Nomura, *Anal. Chim. Acta*, 2002, **468**, 345.
27 Y.-P. Xiong, H. Kishimoto, K. Yamaji, M. Yoshinaga, T. Horita, M. E. Brito and H. Yokokawa, *Electrochem. Solid-State Lett.*, 2010, **13**, B21.
28 H. L. Tuller and A. S. Nowick, *J. Phys. Chem. Solids*, 1977, **38**, 859.
29 U. Holzwarth and N. Gibson, *Nat. Nanotechnol.*, 2011, **6**, 534.
30 D. D. Wagman, J. E. Kilpatrick, W. J. Taylor, K. S. Pitzer and F. D. Rossini, *J. Res. Natl. Bur. Stand.*, 1945, **34**, 143.
31 S. L. Moffitt, Q. Ma, D. B. Buchholz, R. P. H. Chang, M. J. Bedzyk and T. O. Mason, *J. Phys.: Conf. Ser.*, 2016, **712**, 012116.
32 P. Pfalzer, J.-P. Urbach, M. Klemm, S. Horn, M. L. DenBoer, A. I. Frenkel and J. P. Kirkland, *Phys. Rev. B:Condens. Matter Mater. Phys.*, 1999, **60**, 9335.
33 R. C. Lye, J. C. Phillips, D. Kaplan, S. Doniach and K. O. Hodgson, *Proc. Natl. Acad. Sci. U. S. A.*, 1980, **77**, 5884.

 This journal is © the Owner Societies 2026